To be published in Photonics Research:

Title: Total polarization conversion using subwavelength laser-induced periodic surface structures on stainless steel

Authors: Mahmoud Elshorbagy,Luis Miguel Sanchez-Brea,Jeronimo Buencuerpo,Jesus del Hoyo,Ángela Soria-García,Verónica Pastor-Villarrubia,Alejandro San Blas,Ainara Rodriguez,Santiago Olaizola,Javier Alda

Accepted: 18 April 22

Posted 06 May 22

DOI: https://doi.org/10.1364/PRJ.454451

Polarization conversion using customized subwavelength laser-induced periodic surface structures on stainless steel

MAHMOUD H. ELSHORBAGY[1,2], LUIS MIGUEL SÁNCHEZ-BREA[1], JERÓNIMO BUENCUERPO[1,3], JESÚS DEL HOYO[1], ÁNGELA SORIA-GARCÍA[1], VERÓNICA PASTOR-VILLARRUBIA[1], ALEJANDRO SAN-BLAS[4,5], AINARA RODRÍGUEZ[4,5], SANTIAGO MIGUEL OLAIZOLA[4,5], AND JAVIER ALDA[1,*],

[1]*Grupo Complutense de Óptica Aplicada, Departamento de Óptica, Facultad de Ciencias Físicas, Universidad Complutense de Madrid, Plaza de las Ciencias S.N., 28040, Madrid, Spain.*
[2]*Physics Department, Faculty of Science, Minia University, 61519 El-Minya, Egypt.*
[3]*L'Institut Photovoltaïque d'Île-de-France (IPVF), 18 Bd Thomas Gobert, Palaiseau, 91120, France.*
[4] *Ceit-Basque Research and Technology Alliance (BRTA), Manuel Lardizabal 15, 20018 Donostia / San Sebastián, Spain.*
[5]*Universidad de Navarra, Tecnun, Manuel Lardizabal 13, 20018 Donostia / San Sebastián, Spain.*
[*]*Corresponding: javier.alda@ucm.es*

Abstract: Stainless steel is a basic raw material in industry. It can be customized by generating laser-induced periodic surface structures (LIPSS) as subwavelength gratings. Here, we present the capabilities of LIPSS on stainless steel to modify the polarization state of the reflected radiation at the infrared. These structures have been modeled using the finite element method and fabricated by femtosecond laser processing. The Stokes parameters have been obtained experimentally and a model for the shape has been used to fit the simulated Stokes values to the experimental data. The birefringence of the LIPSS is analyzed to explain how they modify the polarization state of the incoming light. We find the geometry of the subwavelength grating that makes it work as an optical retarder that transforms a linearly polarized light into a circularly polarized wave. Also, the geometrical parameters of the LIPSS are tuned to absorb selectively one of the components of the incoming light, becoming a linear axial polarizer. An appropriate selection of the geometrical parameters and orientation of the fabricated LIPSS makes possible to obtain an arbitrary pure polarization state when illuminated by a pure linearly polarized state oriented at an azimuth of 45°. The overall reflectance of these transformations reaches values close to 60% with respect to the incident intensity, that is the same reflectivity obtained for non nanostructured stainless steels flat surfaces.

1. Introduction

The state of polarization of light changes when interacting with anisotropic optical materials. In nature, this capability mostly relies on their atomic/molecular distribution that shows an anisotropy related with their crystalline characteristics [1–4]. Nanostructuring isotropic materials makes possible to tailor their optical response, allowing selective transmission, reflection, or absorption, as a function of wavelength, angle of incidence, and state of polarization [5, 6]. In particular, subwavelength metallic gratings excite surface plasmon resonances using oblique incident light, or cavity resonances at normal incidence [7]. Their use as filters to customize the balance between transmission, reflection, and absorption has been also demonstrated in waveguides and biosensors [8–15]. Regarding materials, silver is selected when looking for a sharp optical response, and gold is preferred in terms of its robustness against environmental

agents, and its biocompatibility [12, 16, 17]. Also, subwavelength structures in steel have been proposed for some applications such as low cost plasmonic devices [18–20], and fabrication of colored surfaces [21]. Nanopatterned steel substrates are also used as templates to fabricate other nanostructured surfaces [22], or directly included in optical systems [23]. However, the capabilities of nanostructured stainless steel for the modification of the polarization state of light still require further research to integrate them into low-cost optical systems. A relevant issue in the practical deployment of these devices is related to the existence of fast and efficient fabrication methods. Typically, electron beam lithography, deep UV-lithography, focused ion beam, and nanoimprinting, combined with a plethora of deposition techniques (sputtering, spin coating, thermal evaporation, etc.), are common tools used to fabricate subwavelength structures [24]. As an alternative for the generation of subwavelength gratings, we used ultrafast laser processing to produce laser-induced periodic surface structures (LIPSS) [25]. Besides its large throughput and low cost, an additional advantage of LIPSS is that the nanostructure is created directly on the surface without postprocessing. The localized nanostructure is generated using pulses with a duration shorter than the thermal relaxation time of the material. This prevents energy to modify surrounding areas. The technique has been demonstrated for laser pulses lasting from femto to picoseconds [26]. However, the fabrication process requires an optimization of the multi-pulse delivery and a spatial control of the irradiated area [27]. This technique has been applied on metals [28, 29], semiconductors [30, 31], dielectrics [32], and thin films [33], indicating its high flexibility and effectiveness.

In this work, we study the optical properties of metallic nanostructures fabricated on stainless steel substrates. The nanostructures studied here present binary and sinusoidal profiles, and are generated by femtosecond laser processing. In section 2, we have tuned the parameters of the sinusoidal profile to fit the simulated Stokes parameters to the experimental values. Section 3 presents the results of the Stokes vectors, Jones matrices, field distribution, and reflectance for binary and sinusoidal profiles in terms of their geometries. The obtained results indicates the possibility of using stainless steel as a promising material for fabricating nanostructured optical components that fulfill both cost and performance terms. Finally, section 4 summarizes the main findings of this contribution.

2. Fabrication, modeling and validation

Our LIPSS are fabricated on top of AISI-304 stainless steel substrates (10×20 mm^2). The detailed fabrication process and optical characterization were presented and discussed previosly [34]. The stainless steel samples studied in this contribution were processed using a Ti:Saphire laser emitting 120 fs pulses at a central wavelength of $\lambda = 800$ nm with a repetition rate of 1 kHz. A cylindrical lens was used to obtain a line-profile in the focal plane with dimensions 6 mm $\times$ 32 μm. The samples were processed at varying irradiation conditions between samples. Fluence 0.2 J/cm^2 was common for all samples, while number of pulses (controlled through the processing speed), ranged between 80 and 240. Two sets of samples have been used in the validation process. These two sets differ in the orientation of the laser beam polarization (parallel or perpendicular) with respect to the direction of the movement during the sample processing. We will call these two sets as I and II for the cases of 0^o orientation and 90^o orientation, respectively.

Samples with different periods (from 590 nm up to 635 nm) were fabricated for sets I and II. The mean height of the structures is kept constant, GH = 125 ± 7 nm. The samples were examined using scanning electron microscope (SEM) for analyzing the surface structure and the geometrical shapes. The images in Figs. 1.a,b,c correspond to the samples of the first set I with periods 606, 612, 631 nm, respectively. The images in Figs. 1.d,e,f correspond to the samples of the set II with periods 591, 606, 612, nm respectively. These SEM images reveal a sinusoidal type periodic grating structure for all samples. At the same time, they show how the periodic structure is significantly altered over lengths of several periods, as it is typical in LIPSS. The

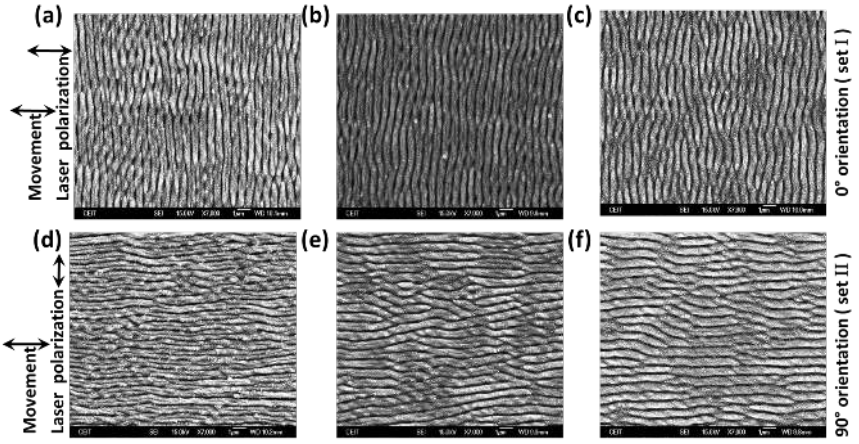

Fig. 1. SEM images for quasi-sinusoidal LIPSS fabricated on top of a steel substrate using femtosecond laser processing. The polarization state of the laser beam is parallel to the direction of the movement during the sample processing for a, b, and c subplots, and perpendicular for d, e, and f.

description given by the SEM images is completed using AFM topography measurements as shown in Fig. 2. In fact, the results from the AFM images can be used to evaluate the values of the height of the profile, GH, along the sample.

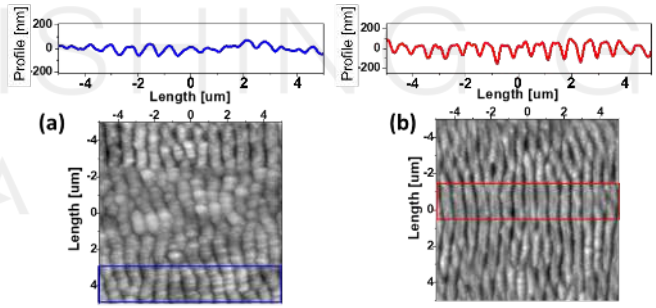

Fig. 2. (a) AFM image and profile for the sample with period P=631 nm from set I. (b) AFM image and profile for the sample with period P=606 nm from set II.

The profile is strongly dependent on the material of the sample, the conditions of the surface [35–38], and even on the substrate temperature [39, 40]. This means that this profile departs from the ideal sinusoidal form. To accurately fit the simulated results of the optical polarization parameters with the experimental values, we need to take this deformation into account by introducing the following profile function:

$$h(x) = \frac{\mathrm{GH}}{2}\left\{1 - 2\left[\frac{1+\cos(2\pi x/P)}{2}\right]^{\beta}\right\}, \tag{1}$$

where, $h(x)$ represent the height at each point along the $x-$axis in the simulated periodic unit cell, GH is the profile height, and P is the period. When the parameter β is equal to 1 we obtain the ideal sinusoidal shape geometry (see Fig. 3.a on top). By changing β we can simulate a flatter profile ($\beta > 1$, see Fig. 3.a at the bottom) or a sharper one ($\beta < 1$, see Fig. 3.a in the middle).

The geometrical parameters of the profile are also shown in Fig. 3.c for the sinusoidal case treated in this section and for the binary profile (see Fig. 3.b). The analysis made in this section, described by Eq. (1), uses $P = \mathrm{BW} + S$, where S is the separation between grating elements, and BW is the width of the base of the sinusoidal profile.

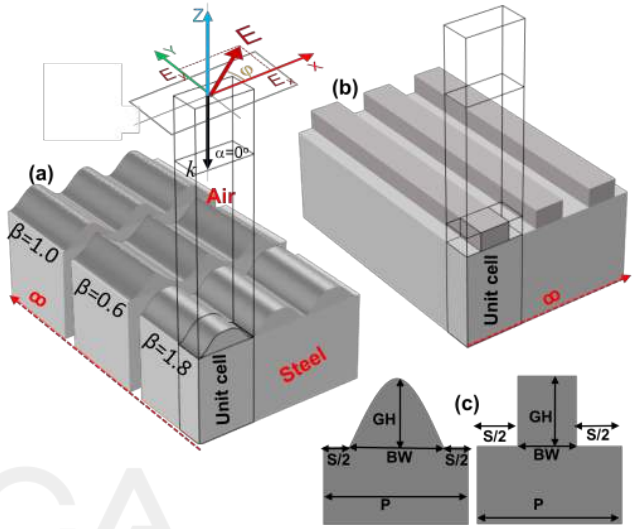

Fig. 3. Subwavelength gratings studied, (a) sinusoidal and (b) binary. They have a period $P = 632$ nm and are made of stainless steel. (c) Transversal sections showing the geometrical parameters of the profiles. In subplot (a) we have included a graphic layout showing the vector and components of the incoming electric field, E, the azimuth angle, φ (in our case $\varphi = 45°$), the wavevector, k, and the XYZ coordinate system (the incidence angle is $\alpha = 0°$ and it is not represented).

Our model uses a plane wave impinging perpendicularly on the substrate ($\alpha = 0^o$ in Fig. 3), and linearly polarized with its electric field oriented at an angle $\varphi = 45^o$, with respect to the $x-$axis, and having an amplitude $(1/\sqrt{2}, 1/\sqrt{2}, 0)$ V/m. The grating is aligned along the $y-$axis and the propagation is along the $z-$direction (perpendicular to the substrate). The wavelength in the simulation, $\lambda = 633$ nm, is the same of the experimental measurement. The optical field distribution along the whole structure has been calculated using Comsol Multiphysics simulation package. The unit cell used in the model has an air layer on top, and a substrate layer (steel) at the bottom (see Fig. 3). The air domain is terminated with a perfect matched layer (PML) on top that simulates an semi-infinite domain. The interface has a shape defined by Eq. (1) and is defined as a dedicated layer having a height equal to GH. The source is located on top of the air domain with its wavevector pointing towards the substrate. The index of refraction of stainless steel is obtained experimentally at $\lambda = 633$ nm as $\tilde{n}_{\mathrm{steel}} = 2.33 + 3.3i$. To represent the LIPSS structure we replicate the previously defined unit cell transversely by applying Floquet periodic boundary conditions along X and Y directions.

This analysis uses the Stokes vector to describe the state of polarization of the reflected light, $S = (I, Q, U, V)$ [41]. I is the intensity of the beam. Q and U represent the balance in power between horizontal and vertical axial polarizations, and linear polarized (LP) light at 45^o and -45^o components, respectively. Finally, V represents the balance between right and left circular polarization (CP) components. These parameters obey the relation $I \geq \sqrt{Q^2 + U^2 + V^2}$, being the equality condition applicable only for pure polarized beams. A normalized version of these parameters can be obtained just by dividing each one by the intensity, I. Then, the Stokes vector becomes $s = (1, q, u, v)$ and the relation among them becomes $1 \geq \sqrt{q^2 + u^2 + v^2}$. In the case

described in this section, as far as we are assuming a perfect 1D grating, these parameters comply with the pure polarization state condition $\sqrt{q^2 + u^2 + v^2} = 1$.

The Stokes parameters of the light reflected by the fabricated structures were measured using an illumination spot of around 2 mm in diameter. The light source was a He-Ne laser (model 1122P, from JD Uniphase) emitting at $\lambda = 633$ nm, with an spectral width lower than 0.002 nm.

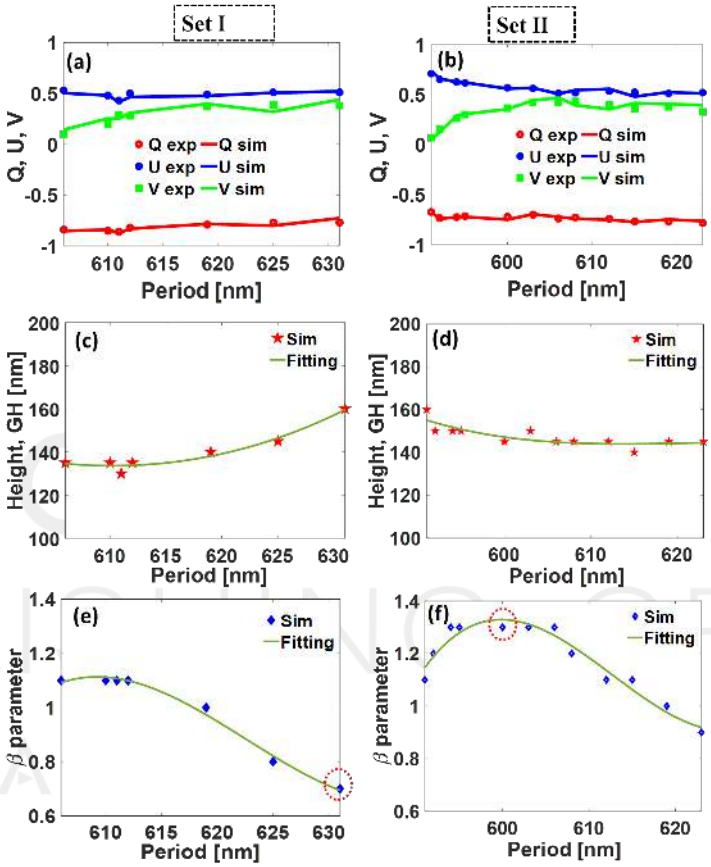

Fig. 4. Fitting of the simulated (solid lines) and experimentally measured (symbols) Stokes parameters for samples fabricated using femtosecond laser ablation with polarization parallel (a), and perpendicular (b) to the direction of the movement during the sample fabrication. Plots (c)-(f) show the geometrical parameters GH and β of the profile that best fit the experimental data for the two sets of samples (set I in (c) and (e), and set II in (d) and (f)). The dashed red circles select the lowest β value on plot (e), and the highest β value on plot (f). The solid lines in plots (c)-(f) represent the cubic polynomial fitting of the geometrical parameters *vs.* P.

The electric field distributions evaluated by Comsol are used to evaluate the Stokes parameters of the reflected light [34, 41]. Individually for each sample, the matching between experimental and simulated Stokes parameters is obtained by changing the geometry of the grating in terms of its height, GH, and shape, β (see Eq.(1)). The result of this fitting is shown in Figs. 4.a and 4.b respectively. The simulated values for the Stokes parameters are represented by solid color lines, while the experimental values are represented by colored symbols.

The values of GH producing a best fitting are presented in Figs. 4.c, and 4.d, for set I and II, respectively. The mean height for set I, and II are $GH_{sim} = 140 \pm 10$ nm, and 147.5 ± 5 nm,

respectively. These values are close to the experimental mean value which is $GH_{exp} = 125 \pm 7$ nm. The shape parameter β that produces the best fitting is presented in Fig. 4.e, and 4.f for set I and II, respectively. The polarization parameters of set I fits better with sharper profiles than set II, meaning that set II seems to have a flatter top portion in the profile. The red dashed circles in Figs 4.e,f correspond to the lowest and highest β values. These two points on the β plots are for the samples measured by atomic force microscopy, AFM (see images in Fig. 2). The profile has a sharper sinusoidal shape in Fig. 2.a, which corresponds to the point highlighted by the red dashed circle on Fig. 4.e. A flat top profile of the LIPSS is obtained in Fig. 2.b, that corresponds to the point highlighted by the red dashed circle on Fig. 4.f. In both cases, the experimental profile images agree with the simulated values for the deformation. The SEM and AFM images show a structure with a localized periodicity that varies along the samples, where the top edges have not an uniform profile. In this case, the values obtained from the simulation can be considered as the overall average for periodicity P, height GH, and top edge deformation β. From these results, we see how the optical model is able to accurately predict the optical response of a non uniform LIPSS structures.

3. Polarization modulation with binary and sinusoidal gratings

To better understand the effect of the geometry of our LIPSS on the modification of the polarization state, besides the sinusoidal profile, we extend our calculations to binary gratings. These binary shape is parameterized by the height of the the profile, GH, and the width of the base, BW. In this section, we focus on how these geometrical parameters change the polarization state of the incoming light. We fix the period in both structures to $P = 632$ nm, that lies within the range of the fabricated ones. Actually, this value can be tuned by changing the fabrication conditions [42, 43]. We have used the same modeling setup used in the previous section, to conduct the calculation of this section. We move our analysis to $\lambda = 808$ nm, $\tilde{n}_{steel} = 2.68 + 3.77i$, because the customized polarizers are important in near-infrared spectroscopy [44]. The performance in power of the LIPSS is described by the value of the reflectance. Here, we remind that the transmittance of the system is zero, and the incoming power is distributed between reflected and absorbed power. As a consequence, a null reflectance is associated with filtering properties of the structure.

Figure 5 represents the normalized Stokes parameters, (q, u, v), of the reflected light and the reflectance as a function of the height GH and the base width BW for the binary profile (left) and the sinusoidal shape (right). In the case of the rectangular profile, BW can be related easily with the fill factor as FF = BW$/P$. The sinusoidal shape is also characterized by the total height, GH, and by the distance between the minima of the profile, GW. The rest of the period not included within the BW range has a height equal to zero, meaning that the period of the sinusoidal grating has only 1 maximum. These calculations consider the shape parameter $\beta = 1$. The geometrical parameters used in this section are also depicted in Fig. 3. The maps in Fig. 5 show some combinations of the geometrical parameters that generate maximum and minimum values of the Stokes parameters. In Fig. 5, we have also represented the reflectivity of the structure. These values should be compared with the reflectivity of a flat surface (no LIPSS) made of the same stainless steel that is $R = 0.6$.

To have them properly identified, we label them with a capital letter: B for binary (rectangular) and S for sinusoidal. Then, a subindex is added to denote the q, u, or v parameters. Finally, a superscript is added as I, II, III, IV, V for a maximum, or minimum locations as shown on the maps of Fig. 5. The geometrical parameters for these locations are given in Tab. 1 for the binary and sinusoidal profiles.

The identification of the maxima and minima in the maps of the Stokes parameters makes possible to select geometrical parameters of the grating that generate a well defined state of polarization. The maximum $q = 1$ corresponds with horizontal linear polarization (0^o LP), and the minimum $q = -1$ is for a vertical linear polarization (90^o LP). The maximum and minimum in

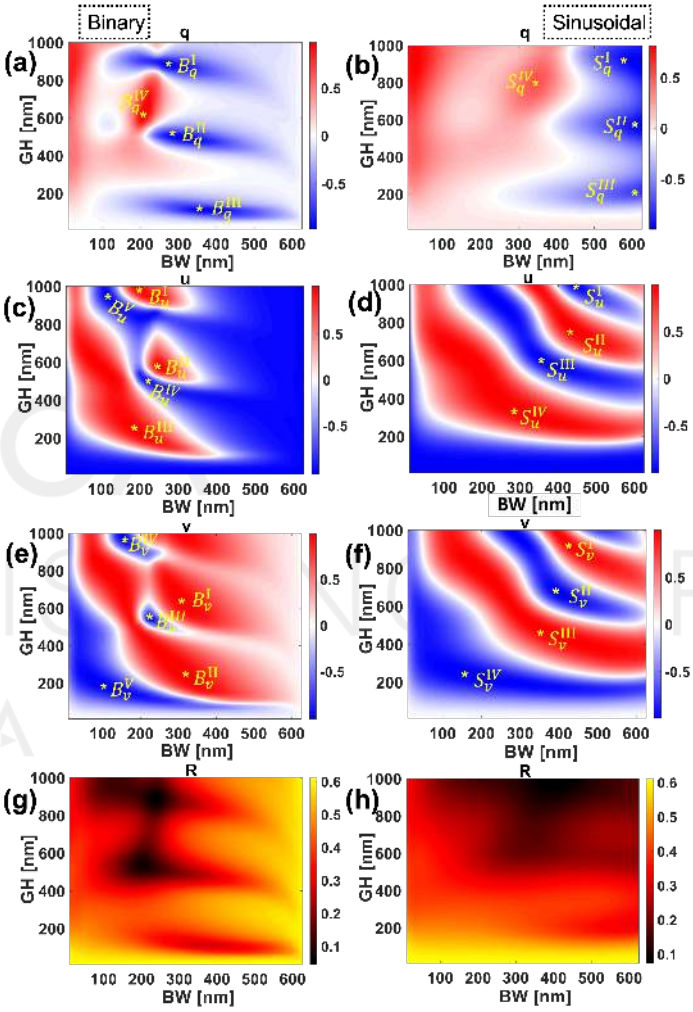

Fig. 5. Maps of the normalized Stokes parameters q, u, and v, and reflectance, R, as a function of the geometrical parameters GH and BW for the binary (left) and sinusoidal (right) gratings. The maximum value of reflectivity, $R_{\max} = 0.6$, is around the reflectivity value given by a regular, not nanostructured, stainless steel surface.

Table 1. Geometrical parameters and reflectance of the selected minima, and maxima for the binary and sinusoidal profiles. The state of polarization of the reflected light is given in the column "Pol. State".

Binary label	GH, BW [nm]	R%	Pol. State	Sinusoidal label	GH, BW [nm]	R%	Pol. State
B_q^I	880, 275	12	90^o LP	S_q^I	905, 615	23	90^o LP
B_q^{II}	500, 300	19.3	90^ol LP	S_q^{II}	570, 620	17.6	90^ol LP
B_q^{III}	110, 375	28	90^o LP	S_q^{III}	220, 625	31.1	90^o LP
B_q^{IV}	615, 210	18	0^o LP	S_q^{IV}	800, 350	14.5	0^o LP
B_u^I	985, 200	16	$+45^o$ LP	S_u^I	995, 445	15.8	-45^o LP
B_u^{II}	580, 250	18.3	$+45^o$ LP	S_u^{II}	770, 440	17.5	$+45^o$ LP
B_u^{III}	245, 185	23.3	$+45^o$ LP	S_u^{III}	600, 360	39	-45^o LP
B_u^{IV}	500, 220	10.2	-45^o LP	S_u^{IV}	340, 295	59	$+45^o$ LP
B_u^V	940, 120	10.2	-45^o LP				
B_v^I	640, 310	37.3	RCP	S_v^I	930, 420	8.7	LCP
B_v^{II}	250, 315	45.5	RCP	S_v^{II}	675, 400	18.7	RCP
B_v^{III}	540, 225	8.7	LCP	S_v^{III}	460, 380	32.2	LCP
B_v^{IV}	975, 155	12.4	LCP	S_v^{IV}	240, 165	46	RCP
B_v^V	200, 95	45.6	LCP				

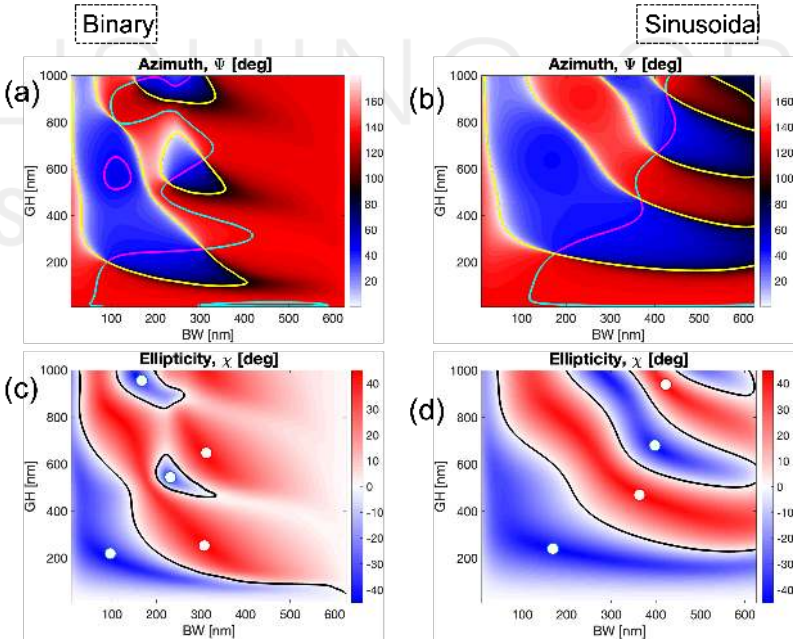

Fig. 6. Maps of the Azimuth, Ψ, and ellipticity, χ, angles as a function of BW and GH parameters for the binary (left column) and sinusoidal (right column) profiles. The contour lines in the azimuth maps represent the values of $\Psi = 45°$ (in magenta), $\Psi = -45° = 135°$ (in cyan), and $\Psi = 0°$ and $\Psi = 180°$ (in yellow). The black contour lines in the ellipticity maps are for a value $\chi = 0°$. The locations of the configurations with $\chi = -45°$ and $\chi = +45°$ are given as white dots in the blue and red regions, respectively.

u ($u = \pm 1$) are for $+45^o$ LP and -45^o LP, respectively. For the v maps we find the maxima $v = 1$ representing left-handed circular polarization (LCP), meanwhile the minima $v = -1$ correspond with the right-handed circular polarization (RCP). A similar consequence can be extracted for the case of sinusoidal grating profiles (see Fig. 5.b,d,f). The corresponding reflectivity of the structure presented in Figs. 5. g,h, which defines the geometrical parameters where the structure works as a filter (minimum reflectivity). A flat stainless steel substrate has a maximum value of reflectivity of $R_{\max} = 0.6$, which is about the same maximum obtained for the structure when including LIPSS, as appear in Figs. 5.g,h.

For the generated light states, we also calculated the azimuth angle:

$$\Psi = 0.5 \tan^{-1}\left(\frac{U}{Q}\right), \tag{2}$$

and the ellipticity angle:

$$\chi = \tan^{-1}\left(\frac{V}{I + \sqrt{Q^2 + U^2}}\right). \tag{3}$$

Azimuth directly represents the rotation angle of the axis of the polarization ellipse, allowing to easily identify horizontal ($\Psi = 0°$), vertical ($\Psi = 90°$) and $\pm 45°$ orientations of the polarization ellipse (see Figs. 6.a and 6.b). The ellipticity angle allows to easily identify linear ($\chi = 0°$) and circular ($\chi = \pm 45°$) polarization states (see Figs. 6.c and 6.d). Also, it allows to exactly know how much the mixed light states are. This combined analysis of the azimuth and ellipticity angles can be made using the contour lines presented in Fig. 6.

The physical mechanisms of the polarization conversion may involve the selective absorption of the field components, and/or additional phase shifts between them. The input field components generate surface currents circulating the structure. Depending on the topography, these currents can be attenuated through Joule dissipation or plasmonic resonances, or they can emit electromagnetic waves with a phase difference between components that is strongly dependent on the geometry. The change in the polarization state can be visualized using 3D plots of the fields obtained by a full wave analysis of the structure during the propagation process. The results of this analysis are shown in Fig. 7 for the binary grating on the left, and sinusoidal on the right plots. The plots use a selection of some points in Tab. 1 to show representative polarization conversion using the binary or sinusoidal gratings. In Fig. 7.a, the location of the source, LIPSS, reflected light, and PML domains are shown using yellow arrows. The reflected light can be axial LP as in Fig. 7.a,b, or ± 45 LP as in Fig. 7.c,d. Finally, the conversion from LP to CP light are shown in Fig. 7.e for the LCP, and Fig. 7.f for the RCP.

The previous analysis is a particular case for just one incident illumination, 45^o linear polarized light. However, in order to totally characterize the polarimetric properties of the LIPSS structure, the polarization matrix of the material must be calculated. Since we assume that LIPSS are periodical, depolarization analysis is not required, so we can use the Jones formalism. Mathematically, this is written as

$$\mathbf{E}_{\text{out}} = \mathbf{P}_{\mathbf{LIPSS}}\, \mathbf{E}_{\text{in}} = \begin{pmatrix} E_{x,\text{out}} \\ E_{y,\text{out}} \end{pmatrix} = \begin{pmatrix} P_{xx} & P_{xy} \\ P_{yx} & P_{yy} \end{pmatrix} \begin{pmatrix} E_{x,\text{in}} \\ E_{y,\text{in}} \end{pmatrix}. \tag{4}$$

In our case, the grating generated as a LIPSS, can be described by the corresponding Jones matrix, $\mathbf{P}_{\text{LIPSS}}$, and the input and output vectors, $\mathbf{E}_{\text{in}}$ and $\mathbf{E}_{\text{out}}$, describe the incident and reflected light beams, respectively. Since the coordinate axis is aligned with the axis of the grating, the matrix becomes diagonal, meaning that $P_{xy} = P_{yx} = 0$. Under these conditions

$$\mathbf{P}_{\text{LIPSS}} = \begin{pmatrix} |P_{xx}| & 0 \\ 0 & |P_{yy}| e^{i\phi} \end{pmatrix}. \tag{5}$$

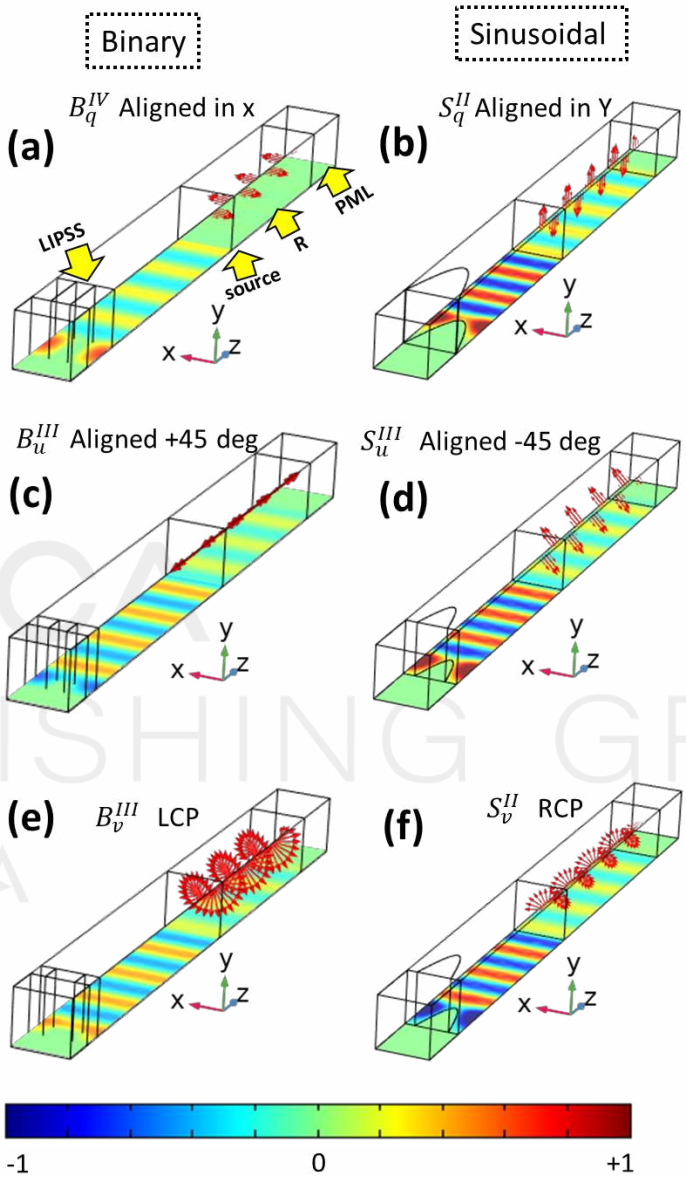

Fig. 7. A full wave propagation of the electric field on LIPSS for (a,c,e) binary grating, and (b,d,f) sinusoidal grating. The yellow arrows in (a) define the location of the source, LIPSS, Reflection, and PML. The electric field in subplot (c) is linearly polarized and oriented along the 45° direction, being the point of view of the graphical representation almost coincident with the direction of the electric field vector. The labels for each field representation corresponds with the cases presented in Table 1 and figure 5. We have also plotted the electric field distributions, along with the field evolution at the output, to help to understand the physical mechanism involved in the conversion.

Then, it is possible to obtain the two non-zero elements of the Jones matrix by just comparing the input and output electric field components

$$|P_{xx}| = |E_{x,\text{out}}/E_{x,\text{in}}|, \tag{6}$$
$$|P_{yy}| = |E_{y,\text{out}}/E_{y,\text{in}}|, \tag{7}$$
$$\phi = \text{angle}(E_{y,\text{out}}) - \text{angle}(E_{x,\text{out}}). \tag{8}$$

Also, the reflectance of the LIPSS can be calculated as

$$R = \frac{1}{2}\left(|P_{xx}|^2 + |P_{yy}|^2\right). \tag{9}$$

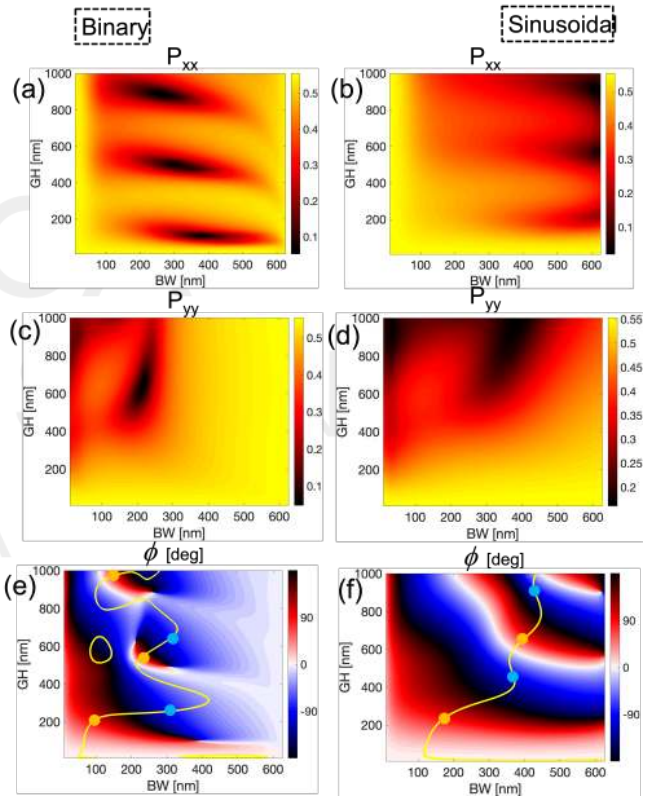

Fig. 8. Maps of the modulus of the elements of the Jones matrix $|P_{xx}|$ and $|P_{yy}|$, and the relative phase shift between the electric field components of the reflected wave, ϕ, in terms of the geometrical parameters GH, and BW. The left column is for the binary profile and the right column is for the sinusoidal shape. The yellow line in the phase map corresponds with the configuration that shows an equal value of the modulus of the diagonal elements of the Jones matrix. The dots are the locations on the $P_{xx} = P_{yy}$ line where $\phi = \pm\pi/2$, i.e., geometries for CP. These dots coincide with those presented in Figs. 6.c and 6.d.

Finally, we calculated these parameters from the simulations shown previously. Figure 8 represents the modulus of P_{xx} and P_{yy}, and the relative phase difference, ϕ, between the components of the reflected electric field for both the rectangular profile (left column) and the sinusoidal profile (right column). These maps are given as a function of the geometric

parameters, GH and BW, of the binary (rectangular) and sinusoidal profile. With Eq. (9) we obtain the maps of the reflectance given in Fig. 5.g,h. The minimum values obtained in $|P_{xx}|$ and $|P_{yy}|$ for the rectangular profile determine the geometrical configuration that generates a linear polarization state along the $y-$axis and $x-$axis, respectively. We can also look for the geometrical configurations having an equal value of the two diagonal elements, $P_{xx} = P_{yy}$, and producing a phase shift $\phi = \pm\pi/2$, because these configurations will generate circular polarized waves. To obtain these configurations we have plotted a yellow line on the phase shift map, that represent the cases where $|P_{xx}| = |P_{yy}|$, blue circle for $\phi = -\pi/2$, and orange circle for $\phi = +\pi/2$. These locations are the ones where the LIPSS behaves as a quarter wave retarder. The Jones analysis shows that, by a proper selection of the LIPSS's geometry and orientation, these systems can transform any pure state of polarization into any other.

4. Conclusions

We show how the fabricated stainless steel LIPSS can produce a change in the state of polarization of an incoming radiation under normal incidence conditions. The Stokes parameters of several experimental samples with different period and height have been measured. These results have been compared to simulations obtained to FEM. The shape of the LIPSS has been tuned in order to match the simulations to the experimental results. The resulting parameters for the fitting are in accordance with the experimental profiles derived from SEM and AFM images.

Once the simulation conditions are validated, we have made a detailed analysis of the LIPSS geometry for binary and sinusoidal shapes to find those configurations that generate a significant variation of the state of polarization of the incoming light. By controlling the steel nanostructure geometry, we can tune the polarization characteristics. These devices can act as wave-retarders or linear polarizers. In fact, we have demonstrated that a customized profile of the LIPSS can generate any polarization state into when illuminated by a linearly polarized beam having an azimuth of 45°. As a summary, we can conclude that the analysis made in this contribution can promote the use of LIPSS on stainless steel to fabricate low-cost retarders and polarization filters.

Funding Information

Ministerio de Economía y Competitividad (Spain) and the European funds for regional development (EU): Retos Colaboración 2019, Teluro-AEI project, RTC2019-007113-3, and by project Nanorooms PID2019-105918GB-I00.

Disclosure and conflic of interest

The authors declare no conflict of interest.

References

1. Y. P. Svirko and N. I. Zheludev, *Polarization of Light in Nonlinear Optics* (Wiley, 2000).
2. D. F. Eaton, "Nonlinear optical materials," Science **253**, 281–287 (1991).
3. V. Lucarini, J. J. Saarinen, K.-E. Peiponen, and E. M. Vartiainen, *Kramers-Kronig relations in optical materials research*, vol. 110 (Springer Science & Business Media, 2005).
4. M. K. Chen, Y. Wu, L. Feng, Q. Fan, M. Lu, T. Xu, and D. P. Tsai, "Principles, functions, and applications of optical meta-lens," Adv. Opt. Mater. **9**, 2001414 (2021).
5. M. B. Ross, C. A. Mirkin, and G. C. Schatz, "Optical properties of one-, two-, and three-dimensional arrays of plasmonic nanostructures," The journal physical chemistry C **120**, 816–830 (2016).
6. J. Alda and G. D. Boreman, *Infrared antennas and resonant structures* (SPIE Press, 2017).
7. J. Zhou and L. J. Guo, "Transition from a spectrum filter to a polarizer in a metallic nano-slit array," Sci. reports **4**, 1–8 (2014).
8. L. Wang and Z. Zhang, "Resonance transmission or absorption in deep gratings explained by magnetic polaritons," Appl. Phys. Lett. **95**, 111904 (2009).
9. J. Zhou and L. J. Guo, "Transition from a spectrum filter to a polarizer in a metallic nano-slit array," Sci. reports **4**, 1–8 (2014).

10. C. Han and W. Y. Tam, "Plasmonic ultra-broadband polarizers based on ag nano wire-slit arrays," Appl. Phys. Lett. **106**, 081102 (2015).
11. C. Lertvachirapaiboon, A. Baba, S. Ekgasit, K. Shinbo, K. Kato, and F. Kaneko, "Transmission surface plasmon resonance techniques and their potential biosensor applications," Biosens. Bioelectron. **99**, 399–415 (2018).
12. A. Polyakov, K. Thompson, S. Dhuey, D. Olynick, S. Cabrini, P. Schuck, and H. Padmore, "Plasmon resonance tuning in metallic nanocavities," Sci. reports **2**, 1–5 (2012).
13. M. Vincenti, D. de Ceglia, M. Grande, A. D'Orazio, and M. Scalora, "Tailoring absorption in metal gratings with resonant ultrathin bridges," Plasmonics **8**, 1445–1456 (2013).
14. H. Yan, L. Huang, X. Xu, S. Chakravarty, N. Tang, H. Tian, and R. T. Chen, "Unique surface sensing property and enhanced sensitivity in microring resonator biosensors based on subwavelength grating waveguides," Opt. express **24**, 29724–29733 (2016).
15. N. Kazanskiy, M. Butt, and S. Khonina, "Silicon photonic devices realized on refractive index engineered subwavelength grating waveguides-a review," Opt. & Laser Technol. **138**, 106863 (2021).
16. P. Dong, Y. Wu, W. Guo, and J. Di, "Plasmonic biosensor based on triangular au/ag and au/ag/au core/shell nanoprisms onto indium tin oxide glass," Plasmonics **8**, 1577–1583 (2013).
17. D. V. Nesterenko and Z. Sekkat, "Resolution estimation of the au, ag, cu, and al single-and double-layer surface plasmon sensors in the ultraviolet, visible, and infrared regions," Plasmonics **8**, 1585–1595 (2013).
18. P. R. West, S. Ishii, G. V. Naik, N. K. Emani, V. M. Shalaev, and A. Boltasseva, "Searching for better plasmonic materials," Laser & Photonics Rev. **4**, 795–808 (2010).
19. L. Polavarapu and L. M. Liz-Marzán, "Towards low-cost flexible substrates for nanoplasmonic sensing," Phys. Chem. Chem. Phys. **15**, 5288–5300 (2013).
20. M. Seo, J. Lee, and M. Lee, "Grating-coupled surface plasmon resonance on bulk stainless steel," Opt. express **25**, 26939–26949 (2017).
21. M. S. Ahsan, F. Ahmed, Y. G. Kim, M. S. Lee, and M. B. Jun, "Colorizing stainless steel surface by femtosecond laser induced micro/nano-structures," Appl. surface science **257**, 7771–7777 (2011).
22. T.-F. Yao, P.-H. Wu, T.-M. Wu, C.-W. Cheng, and S.-Y. Yang, "Fabrication of anti-reflective structures using hot embossing with a stainless steel template irradiated by femtosecond laser," Microelectron. Eng. **88**, 2908–2912.
23. P. Boillot and J. Peultier, "Use of stainless steels in the industry: recent and future developments," Procedia engineering **83**, 309–321 (2014).
24. L. Chi, *Nanotechnology: volume 8: nanostructured surfaces* (John Wiley & Sons, 2010).
25. J. Bonse, A. Rosenfeld, and J. Krüger, "On the role of surface plasmon polaritons in the formation of laser-induced periodic surface structures upon irradiation of silicon by femtosecond-laser pulses," J. Appl. Phys. **106**, 104910 (2009).
26. A. Y. Vorobyev and C. Guo, "Direct femtosecond laser surface nano/microstructuring and its applications," Laser & Photonics Rev. **7**, 385–407 (2013).
27. M. Birnbaum, "Semiconductor surface damage produced by ruby lasers," J. Appl. Phys. **36**, 3688–3689 (1965).
28. M. J. Cherukara, K. Sasikumar, A. DiChiara, S. J. Leake, W. Cha, E. M. Dufresne, T. Peterka, I. McNulty, D. A. Walko, H. Wen, S. J. R. S. Sankaranarayanan, and R. J. Harder, "Ultrafast three-dimensional integrated imaging of strain in core/shell semiconductor/metal nanostructures," Nano letters **17**, 7696–7701 (2017).
29. C. Byram, S. S. B. Moram, A. K. Shaik, and V. R. Soma, "Versatile gold based sers substrates fabricated by ultrafast laser ablation for sensing picric acid and ammonium nitrate," Chem. Phys. Lett. **685**, 103–107 (2017).
30. A. Y. Zhizhchenko, P. Tonkaev, D. Gets, A. Larin, D. Zuev, S. Starikov, E. V. Pustovalov, A. M. Zakharenko, S. A. Kulinich, S. Juodkazis, A. A. Kuchmizhak, and S. V. Makarov, "Light-emitting nanophotonic designs enabled by ultrafast laser processing of halide perovskites," Small **16**, 2000410 (2020).
31. M. Sanz, M. Lopez-Arias, J. F. Marco, R. de Nalda, S. Amoruso, G. Ausanio, S. Lettieri, R. Bruzzese, X. Wang, and M. Castillejo, "Ultrafast laser ablation and deposition of wide band gap semiconductors," The J. Phys. Chem. C **115**, 3203–3211 (2011).
32. A. Rudenko, J.-P. Colombier, S. Höhm, A. Rosenfeld, J. Krüger, J. Bonse, and T. E. Itina, "Spontaneous periodic ordering on the surface and in the bulk of dielectrics irradiated by ultrafast laser: A shared electromagnetic origin," Sci. reports **7**, 1–14 (2017).
33. A. Cerkauskaite, R. Drevinskas, A. Solodar, I. Abdulhalim, and P. G. Kazansky, "Form-birefringence in ito thin films engineered by ultrafast laser nanostructuring," ACS Photonics **4**, 2944–2951 (2017).
34. A. San-Blas, M. Martinez-Calderon, J. Buencuerpo, L. M. Sanchez-Brea, J. Del Hoyo, M. Gómez-Aranzadi, A. Rodríguez, and S. Olaizola, "Femtosecond laser fabrication of lipss-based waveplates on metallic surfaces," Appl. surface science **520**, 146328 (2020).
35. J. Sipe, J. F. Young, J. Preston, and H. Van Driel, "Laser-induced periodic surface structure. i. theory," Phys. Rev. B **27**, 1141 (1983).
36. A. Vorobyev and C. Guo, "Enhanced absorptance of gold following multipulse femtosecond laser ablation," Phys. Rev. B **72**, 195422 (2005).
37. C. Florian, S. V. Kirner, J. Krüger, and J. Bonse, "Surface functionalization by laser-induced periodic surface structures," J. Laser Appl. **32**, 022063 (2020).
38. M. Prudent, F. Bourquard, A. Borroto, J.-F. Pierson, F. Garrelie, and J.-P. Colombier, "Initial morphology and feedback effects on laser-induced periodic nanostructuring of thin-film metallic glasses," Nanomaterials **11**, 1076

(2021).
39. S. Gräf, C. Kunz, S. Engel, T. J.-Y. Derrien, and F. A. Müller, "Femtosecond laser-induced periodic surface structures on fused silica: The impact of the initial substrate temperature," Materials **11**, 1340 (2018).
40. Q. Li, Q. Wu, Y. Li, C. Zhang, Z. Jia, J. Yao, J. Sun, and J. Xu, "Femtosecond laser-induced periodic surface structures on lithium niobate crystal benefiting from sample heating," Photonics Res. **6**, 789–793 (2018).
41. E. Collett, "Field guide to polarization," (Spie Bellingham, WA, 2005).
42. E. Skoulas, A. Manousaki, C. Fotakis, and E. Stratakis, "Biomimetic surface structuring using cylindrical vector femtosecond laser beams," Sci. reports **7**, 1–11 (2017).
43. N. Livakas, E. Skoulas, and E. Stratakis, "Omnidirectional iridescence via cylindrically-polarized femtosecond laser processing," Opto-Electronic Adv. **3**, 190035–1 (2020).
44. H. W. Siesler, Y. Ozaki, S. Kawata, and H. M. Heise, *Near-infrared spectroscopy: principles, instruments, applications* (John Wiley & Sons, 2008).